



# System-based investigation on 4-DOF ship maneuvering with hydrodynamic derivatives determined by RANS simulation of captive model tests

Hai-peng Guo<sup>a,b</sup>, Zao-jian Zou<sup>a,b,\*</sup>

<sup>a</sup> State Key Laboratory of Ocean Engineering, Shanghai Jiao Tong University, Shanghai 200240, China

<sup>b</sup> School of Naval Architecture, Ocean and Civil Engineering, Shanghai Jiao Tong University, Shanghai 200240, China



## ARTICLE INFO

### Article history:

Received 13 August 2016

Received in revised form 31 May 2017

Accepted 7 August 2017

Available online 30 August 2017

### Keywords:

Ship maneuverability

4-DOF

System-based method

CFD

## ABSTRACT

For the non-negligible roll-coupling effect on ship maneuvering motion, a system-based method is used to investigate 4-DOF ship maneuvering motion in calm water for the ONR tumblehome model. A 4-DOF MMG model is employed to describe ship maneuvering motion including surge, sway, roll, and yaw. Simulations of circular motion test, static drift and heel tests are performed by solving the Reynolds-averaged Navier-Stokes (RANS) equations, after a convergence study quantifying the necessary grid spacing and time step to resolve the flow field adequately. The local flow field is analyzed for the selected cases, and the global hydrodynamic forces acting on the ship model are compared with the available experiment data. Hydrodynamic derivatives relating to sway velocity, yaw rate, and heel angle are computed from the computed force/moment data using least square method, showing good agreement with those obtained from EFD data overall. In order to investigate further the validity of these derivatives, turning circle and zigzag tests are simulated by using the 4-DOF MMG model with these derivatives. The trajectories and the time histories of the kinematic variables show satisfactory agreement with the data of free-running model tests, indicating that the system-based method coupled with CFD simulation has promising capability to predict the 4-DOF ship maneuvering motion for the unconventional vessel.

© 2017 Elsevier Ltd. All rights reserved.

## 1. Introduction

Ship maneuverability is a major hydrodynamic performance involving navigational safety and efficiency. With the promulgation of IMO's standards for ship maneuverability (IMO, [1,2]), there is a growing demand of assessing maneuverability in design stage. Previously, most studies focused on 3 degrees of freedom (DOF) maneuvering motion including surge, sway, and yaw in the horizontal plane. However, it is well known that for vessels with high service speed and small metacentric height such as surface combatant, large container ship and passenger ship, obvious roll motion can be observed during maneuvering especially hard turning (Yasukawa and Yoshimura [3]). For such vessels, the influence of roll motion on the ship maneuvering motion is not negligible, and it is necessary to investigate 4-DOF ship maneuvering motion by taking roll-coupling effect into account.

System-based and CFD-based methods are major methods for predicting ship maneuverability. The CFD-based method is a full time-domain simulation method of the free-running maneuvers with RANS/DES solver. The free maneuvers of turning circle and zigzag tests were simulated by el Moctar et al. [4] for a twin screw ship with discretized propeller using STAR-CCM+, Broglia et al. [5,6] and Dubbioso et al. [7] for a tanker-like ship model with an actuator disk model using  $\chi$ navis, Carrica et al. [8] for the surface combatant 5415 model with an actuator disk model using CFDSHIP-Iowa. Even though the CFD-based method can obtain rich details of flow during maneuvers, it is very computing resource and time consuming.

Different from direct simulation of CFD-based method, system-based method performs maneuvers simulation by solving the prescribed mathematical model. Several mathematical models have been proposed, such as Abkowitz model (Abkowitz [9]), MMG model (Hirano and Takashina [10], Son and Nomoto [11], and Umeda and Hashimoto [12]). The hydrodynamic derivatives and the interaction coefficients among hull, propeller, and rudder in these models are usually obtained from captive model tests. However, the experiments performed in physical basin have disadvantages such as expensive facilities and complex experimental

\* Corresponding author at: State Key Laboratory of Ocean Engineering, Shanghai Jiao Tong University, Shanghai 200240, China.

E-mail address: [zjzou@sjtu.edu.cn](mailto:zjzou@sjtu.edu.cn) (Z.-j. Zou).

settings, and difficulty in getting insight into the physical mechanisms of the flow field around a ship in maneuvering motion. Therefore, as the CFD tool becomes available, using CFD simulation instead of experiment has drawn more and more attention. Although it is unpractical to carry out direct simulation of free-running maneuvers, CFD method has promising application in simulation of captive model tests. Atsavapranee et al. [13] and Dai and Miller [14] conducted steady turning simulations for a surface combatant 5617 with the RANS solver in CFDShip-Iowa. Static and dynamic planar motion mechanism (PMM) simulations were performed by Sakamoto et al. [15,16] for an unappended surface combatant 5415 model using an URANS/DES solver in CFDShip-Iowa. Shenoi et al. [17,18] for a container ship S175 model, Mucha and el Moctar [19] for a tanker KVLCC2 model using the RANS solver in STAR-CCM+, Mousaviraad et al. [20] for the ONR tumble-home under different head winds condition using the RANS solver in CFDShip-Iowa. Miyazaki et al. [21] and Sung et al. [22] simulated oblique towing and circular motion test (CMT) for KVLCC2 model using the RANS solver in SURF and STAR-CCM+ separately. Cura-Hochbaum and Uharek [23] conducted static and dynamic PMM simulations for KCS model using the RANS solver of Neptuno. For maneuvering prediction using MMG model, accurate determination of the hull-propeller-rudder interaction coefficients is the key issue. Nowadays, it is still challenging to obtain accurately these coefficients by using CFD method, and there are only few publications in this respect. Sakamoto and Kume [24] presented the simulation of captive model test for KVLCC2 model with the RANS solver in SURF to compute the hydrodynamic derivatives and the hull-propeller-rudder interaction coefficients, and zigzag test was simulated using the computed hydrodynamic derivatives and the hull-propeller-rudder interaction coefficients. Overall, it is feasible to obtain the hydrodynamic derivatives and even the hull-propeller-rudder interaction coefficients with simulation of captive model tests based on CFD method.

The present study aims to investigate ship maneuvering motion in the horizontal plane by taking the roll-coupling effect into account. The system-based method with MMG model is used, where the hydrodynamic derivatives and the hull-propeller-rudder interaction coefficients are determined by CFD simulation of captive model tests. A surface combatant ONR tumblehome (ONRT) model is taken as the study object. Static drift test and CMT are simulated to obtain the hydrodynamic derivatives for oblique moving and turning motions, while static heel test is simulated to obtain the derivatives relating to ship heeling. The free maneuvers of turning circle and zigzag tests are simulated with the hydrodynamic derivatives and the hull-propeller-rudder interaction coefficients derived from CFD data, and the simulation results of trajectory, time histories of velocities and roll angle, and maneuverability parameters of turning circle and zigzag tests are compared with the published data of free-running model tests.

## 2. Mathematical model

With all coupled motions concerned, a ship can be considered as a rigid body with 6-DOF motions, including surge, sway, heave, roll, pitch and yaw. For investigating maneuverability of a surface ship with roll-coupling effect being taken into account, the heave and pitch motions can be neglected, and the ship motions can be presented by equations of 4-DOF motions. In this paper, to describe the 4-DOF ship maneuvering motion, two coordinate systems as shown in Fig. 1 are adopted: (a) an earth-fixed coordinate system; and (b) a coordinate system of horizontal body axes with its origin fixed at the ship's center of gravity, the  $x$ -axis pointing toward the bow, the  $y$ -axis to starboard, and the  $z$ -axis downward.

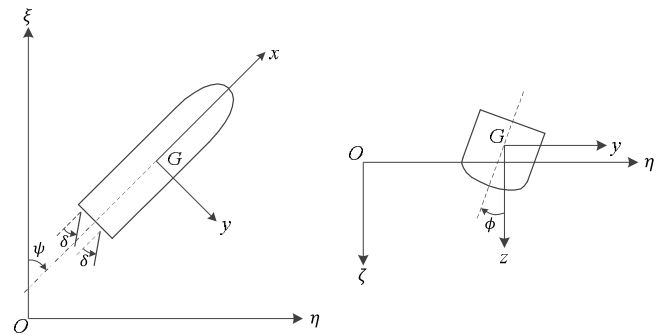


**Fig. 1.** Coordinate systems for 4-DOF mathematical model.

In the coordinate system of horizontal body axes, the 4-DOF ship maneuvering motion can be described by the following equation:

$$\left. \begin{array}{l} m(\dot{u} - vr) = X \\ m(\dot{v} + ur) = Y \\ I_x \dot{p} = K \\ I_z \dot{r} = N \end{array} \right\} \quad (1)$$

where  $m$  is the mass of the ship;  $u$  and  $v$  are the velocity components in the longitudinal and transverse directions, and  $X$  and  $Y$  are the corresponding force components;  $p$  and  $r$  are the angular velocities of roll and yaw motions,  $K$  and  $N$  are the roll and yaw moments, and  $I_x$  and  $I_z$  are the corresponding moments of inertia.

By substituting the expressions for the forces and moments into Eq. (1), a 4-DOF mathematical model can be obtained. In the present study, the following 4-DOF MMG mathematical model proposed by Umeda and Hashimoto [12] is used for the system-based simulation:

$$\begin{aligned} (m + m_x)\dot{u} - (m + m_y)v &= -R(u) + X_{vv}(u)vv \\ + X_{vr}(u)vr + X_{rr}(u)rr + X_P(u, n) + X_R(\delta, u, v, r) & \end{aligned} \quad (2)$$

$$\begin{aligned} (m + m_y)\dot{v} + (m + m_x)ur &= Y_v(u)v + Y_r(u)r + Y_\phi(u)\phi \\ + Y_{vvv}(u)vvv + Y_{vvr}(u)vvr + Y_{vrr}(u)vrr + Y_{rrr}(u)rrr \\ + Y_P(u, v, r) + Y_R(\delta, u, v, r) & \end{aligned} \quad (3)$$

$$\begin{aligned} (I_x + J_x)\dot{p} &= m_x z_H ur + K_v(u)v + K_p(u)p + K_r(u)r + K_\phi(u)\phi \\ - mg\bar{GZ}(\phi) + K_{vvv}(u)vvv + K_{vvr}(u)vvr + K_{vrr}(u)vrr \\ + K_{rrr}(u)rrr + K_P(u, v, r) + K_R(\delta, u, v, r) & \end{aligned} \quad (4)$$

$$\begin{aligned} (I_z + J_z)\dot{r} &= N_v(u)v + N_p(u)p + N_r(u)r + N_\phi(u)\phi \\ + N_{vvv}(u)vvv + N_{vvr}(u)vvr + N_{vrr}(u)vrr \\ + N_{rrr}(u)rrr + N_P(u, v, r) + N_R(\delta, u, v, r) & \end{aligned} \quad (5)$$

where  $m_x$ ,  $m_y$ ,  $J_x$ , and  $J_z$  are the added masses and added moments of inertia;  $R$  is the ship resistance;  $n$  is the propeller revolutions,  $\delta$  is the rudder angle;  $\phi$  is the heel angle;  $z_H$  denotes the  $z$ -coordinate of the acting point of the sway force;  $g$  is the gravitational acceleration;  $\bar{GZ}$  is the righting arm; the subscripts "P" and "R" denote the force and moment components induced by propeller and rudder.  $X$ ,  $Y$ ,  $K$ , and  $N$  with subscripts  $v$ ,  $r$ , or  $\phi$  are the hydrodynamic derivatives relating to  $v$ ,  $r$ , or  $\phi$ . Here the relation between the roll moment  $K$  and the sway force  $Y$  is assumed to be linear:

$$[K_v, K_r, K_{vvv}, K_{vvr}, K_{vrr}, K_{rrr}] = z_H [Y_v, Y_r, Y_{vvv}, Y_{vvr}, Y_{vrr}, Y_{rrr}] \quad (6)$$

The longitudinal force of propeller  $X_P$  is described by Eq. (7). It is worth noting that the lateral force  $Y_P$  generated by the rotating propeller is relevant to the total hydrodynamic forces acting on the ship during maneuvers. Referring to the related research of Broglia et al. [5],  $Y_P$  can be expressed with the relation including drift angle and yaw rate, as given in Eq. (9). Correspondingly, the roll and yaw moments induced by the propeller are presented as shown in Eqs. (10) and (11).

$$X_P(u, n) = (1 - t_P) \rho n^2 D_p^4 K_T(J) \quad (7)$$

$$J = (1 - w_P) u / n D_p \quad (8)$$

$$Y_P(u, v, r) = \rho n^2 D_p^4 c_{YP} (\beta - l'_P r') \quad (9)$$

$$K_P(u, v, r) = z_P Y_P(u, v, r) \quad (10)$$

$$N_P(u, v, r) = x_P Y_P(u, v, r) \quad (11)$$

where  $t_P$  is the thrust deduction factor,  $\rho$  is the water density,  $D_p$  is the diameter of propeller,  $K_T$  is the thrust coefficient and can be expressed as a 2nd polynomial function of propeller advance ratio  $J$ ;  $c_{YP}$  is the hydrodynamic derivative of the lateral force for the propeller,  $\beta$  is the drift angle,  $r'$  is the normalized yaw rate,  $l'_P$  is the correction factor for the lateral velocity due to yaw rate;  $z_P$  and  $x_P$  are the vertical and longitudinal positions of propeller, respectively.

The rudder force and moment  $X_R$ ,  $Y_R$ ,  $K_R$ , and  $N_R$  can be expressed by the combination of interaction factors and rudder normal force. For the twin-screw ship type, the rudder force model proposed by Lee et al. [25] is given in Eqs. (12)–(15), where the subscripts of 'p' and 's' in parenthesis ')' refer to portside and starboard of the twin-screw ship, respectively.

$$X_R(\delta, u, v, r) = -(1 - t_R)(F_N(p) + F_N(s)) \sin \delta \quad (12)$$

$$Y_R(\delta, u, v, r) = -(1 + a_H)(F_N(p) + F_N(s)) \cos \delta \cos \phi \quad (13)$$

$$K_R(\delta, u, v, r) = z_{HR}(1 + a_H)(F_N(p) + F_N(s)) \cos \delta \quad (14)$$

$$N_R(\delta, u, v, r) = -(x_R + a_H x_H)(F_N(p) + F_N(s)) \cos \delta \cos \phi \quad (15)$$

where  $F_N$  is the rudder normal force.  $t_R$  is the steering resistance deduction factor, defining the deduction of rudder resistance during steering.  $a_H$  is the rudder force increase factor, indicating the additional lateral force acting on the ship by steering.  $z_{HR}$  is the vertical position of the center of effective rudder force.  $x_R$  is the longitudinal position of rudder, while  $x_H$  denotes the longitudinal acting point of the additional lateral force component.

For the twin-screw ship type, the rudder normal force  $F_N$  is expressed as Eqs. (16)–(19).

$$\begin{aligned} F_N \left\{ \begin{array}{c} p \\ s \end{array} \right\} &= \frac{1}{2} \rho A_R \left( u_R^2 + v_R^2 \left\{ \begin{array}{c} p \\ s \end{array} \right\} \right) \\ &\quad \frac{6.13 A_R}{A_R + 2.25} \sin \alpha_R \left\{ \begin{array}{c} p \\ s \end{array} \right\} \end{aligned} \quad (16)$$

$$\alpha_R \left\{ \begin{array}{c} p \\ s \end{array} \right\} = \delta \pm |v_{RP}| / u_R - v_R \left\{ \begin{array}{c} p \\ s \end{array} \right\} / u_R \quad (17)$$

$$u_R = \varepsilon(1 - w_P) u \quad (18)$$

$$\sqrt{\eta}$$

$$v_R \left\{ \begin{array}{c} p \\ s \end{array} \right\} = \frac{U}{2} \left\{ \gamma_R^+ [\beta + |\beta| - l_R^+ (r' + |r'|)] + \gamma_R^- [\beta - |\beta| - l_R^- (r' - |r'|)] \right\} \quad (19)$$

where  $A_R$  is the rudder area,  $\Lambda_R$  is the rudder aspect ratio,  $v_{RP}$  is the lateral rudder inflow velocity induced by propeller rotation;  $\varepsilon$  is a ratio of wake fraction at rudder position to that at propeller position,  $\eta$  is introduced to express the percentage of rudder area in propeller race, which is evaluated by relative propeller-rudder position;  $\kappa$  is the interaction factor between propeller and rudder;  $U$  is the resultant velocity,  $\gamma_R^+$  and  $\gamma_R^-$  represent the flow straightening coefficients for windward and leeward respectively; Likewise,  $l_R^+$  and  $l_R^-$  are the correction factor of flow-straightening effect due to yaw rate.

### 3. Numerical method

In this study, computations are performed with the RANS solver of the CFD platform STAR-CCM+. The RANS equations are closed by means of the isotropic blended SST  $k-\omega$  turbulence model. Accordingly, all-Y<sup>+</sup> treatment is selected for near-wall modeling, which is a hybrid treatment employing wall function for coarse meshes and resolving viscous sub-layer for fine meshes. The governing equations are discretized using the Finite Volume Method (FVM). The convection term is discretized with a second-order upwind scheme; the diffusion term is discretized with a second-order scheme; the temporal terms are discretized using a first-order backwards Euler scheme. The pressure/velocity coupling is solved by SIMPLE method. The two-phase Volume of Fluid (VOF) technique is adopted for capturing the free surface. The Dynamic Fluid Body Interaction (DFBI) module is adopted for the simulation of captive model tests. The earth-fixed and ship-fixed coordinate systems are applied to describe the ship motion. The desired motions are implemented in the earth-fixed coordinate system by moving the whole computational domain, and the grid velocities are defined according to the considered motion.

#### 3.1. Case study

During the recent years, a large amount of CFD simulations relating to ship maneuvering have been carried out for conventional ships appended with a single propeller and single rudder, such as container ship KCS, tanker KVLCC etc. However, there are only a few studies on maneuverability of unconventional vessel types. In this study, the ONR tumblehome (ONRT) vessel published by the US Office of Naval Research, a hypothetical surface combatant publicly accessible for fundamental research, is selected as the subject object. It is a kind of twin screw ship, appended with skeg, bilge keels, shafts and struts. Particularly, the vessel has a wave-piercing hull design with 10° tumblehome sides and transom stern, thus it is known as an unconventional vessel. A large amount of captive and free-running model tests were conducted for the ONRT at the National Research Institute of Fisheries Engineering (NRIFE) [26,27] and Iowa Institute of Hydraulic Research (IIHR) [28,29]. Abundant experimental data are available and can be used to verify the feasibility of the method adopted in the present study. The body plan and centerline profile of the vessel are shown in Fig. 2, and its principal particulars are listed in Table 1. The scale ratio of the model is 48.94:1.

#### 3.2. Computational domain and grid

For CFD simulation, the computation accuracy is highly dependent on the size of computational domain, wall treatment and grid number, which should be properly chosen according to the study object. In order to reasonably solve the flow field around the vessel in maneuvering motion, a cuboid computational domain is chosen, as shown in Fig. 3. The origin of the ship-fixed coordinate system  $O_0-X_0Y_0Z_0$  in CFD computation is defined at the ship's center of

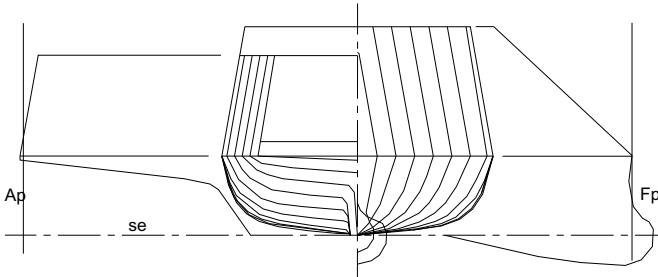


**Fig. 2.** Body plan and centerline profile of the ONR tumblehome (Sadat-Hosseini et al. [27]).

**Table 1**

Principal particulars of the ONR tumblehome (Sadat-Hosseini et al. [27]).

Designation	Full scale	Model scale
Length: $L$	154.0 m	3.147 m
Breadth: $B$	18.78 m	0.384 m
Draft: $T$	5.94 m	0.112 m
Displacement: $\Delta$	8507 ton	72.5 kg
Longitudinal position of center of gravity from midship: $x_{CG}$	2.587 m aft	0.053 m aft
Meta-centric height: $GM$	2.068 m	0.0423 m
Roll radius of gyration: $k_x/L$	0.054	0.054
Pitch and yaw radius of gyration: $k_y/L$ and $k_z/L$	0.250	0.246
Rudder area: $A_R$	$2 \times 28.639 \text{ m}^2$	$2 \times 0.012 \text{ m}^2$
Maximum rudder angle: $\delta_{\max}$	$\pm 35^\circ$	$\pm 35^\circ$

gravity, with  $X_0$ -axis pointing toward stern,  $Y_0$ -axis to starboard, and  $Z_0$ -axis upward. The size of the computational domain ranges  $-1.3L < X_0 < 4L$ ,  $-2L < Y_0 < 2L$ ,  $-0.6L < Z_0 < 0.6L$ . For boundary conditions, the no-slip condition is applied on the solid surfaces of hull

and appendages. The velocity inlet boundaries with zero pressure gradients are imposed on the surfaces of the cuboid computational domain to describe the flow in far field, and the VOF wave damping is set on the surfaces of the computational domain except for the top and bottom sides to reduce the wave oscillation.

The computational domain is discretized using an unstructured hexahedral grid, meanwhile, denser grid around the ship and waterline is used to capture the flow and wave features during ship motion, as shown in Fig. 3. On the surfaces of hull and appendages, prismatic cells are used to achieve better resolution of the near-wall flow and boundary layer. The alignment of these cells is chosen in accordance with the targeted non-dimensional distance from the wall  $Y^+$  ranging from 30 to 60. The surface refinement for the bow, bilges, skeg, struts, and shafts is implemented to reduce loss of model geometry, as shown in Fig. 4.

### 3.3. Convergence study

With the methodology presented by Stern et al. [30], Xing and Stern [31], the convergence study of grid spacing and time step is performed. It can provide an insight into the impact of grid spacing and time step on prediction of ship hydrodynamic performance during maneuvering. The static drift test of  $\beta = 10^\circ$  and static heel test of  $\phi = 10^\circ$  under a nominal speed corresponding to  $Fr = 0.2$  are selected for convergence study. Besides, the convergence is investigated not only for surge force but also for sway force, roll and yaw moments, which are significantly important for ship maneuverability prediction.

#### 3.3.1. Grid spacing

In the grid spacing convergence study, all grid points are given as a percentage of the base size, which are changed systematically with a constant ratio to obtain grids of different density. Three

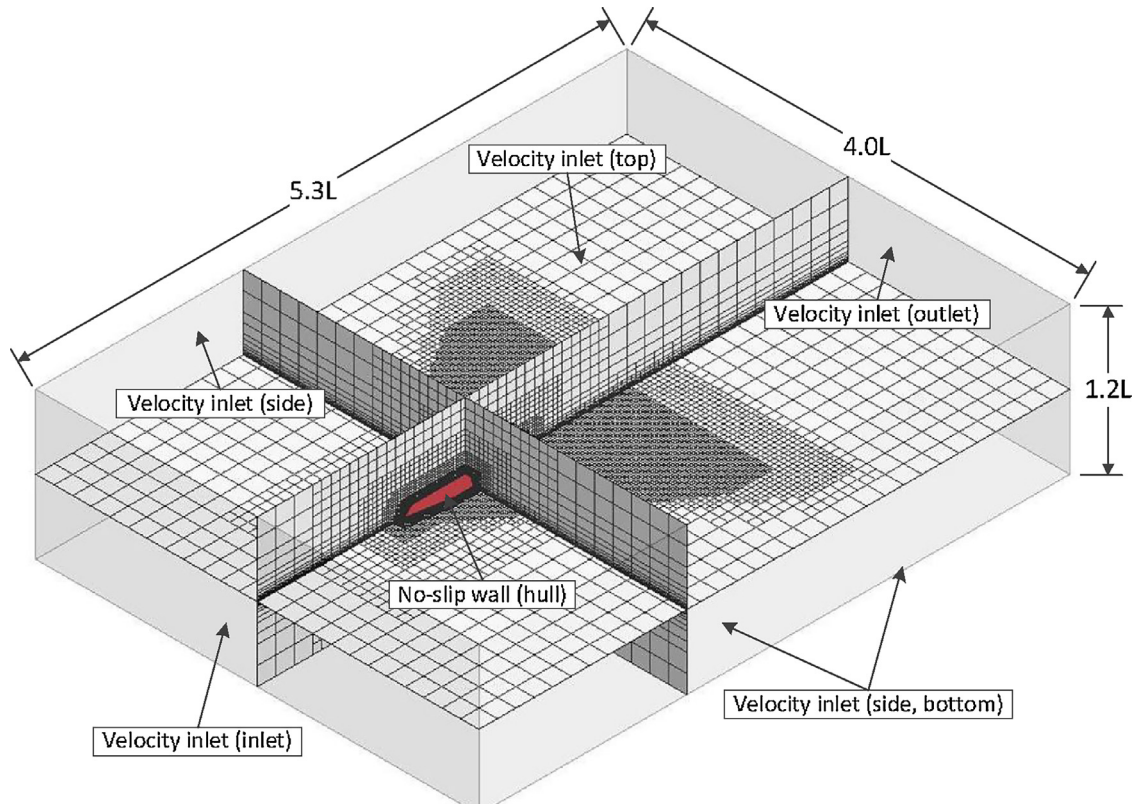


**Fig. 3.** CFD computational domain and boundary conditions.

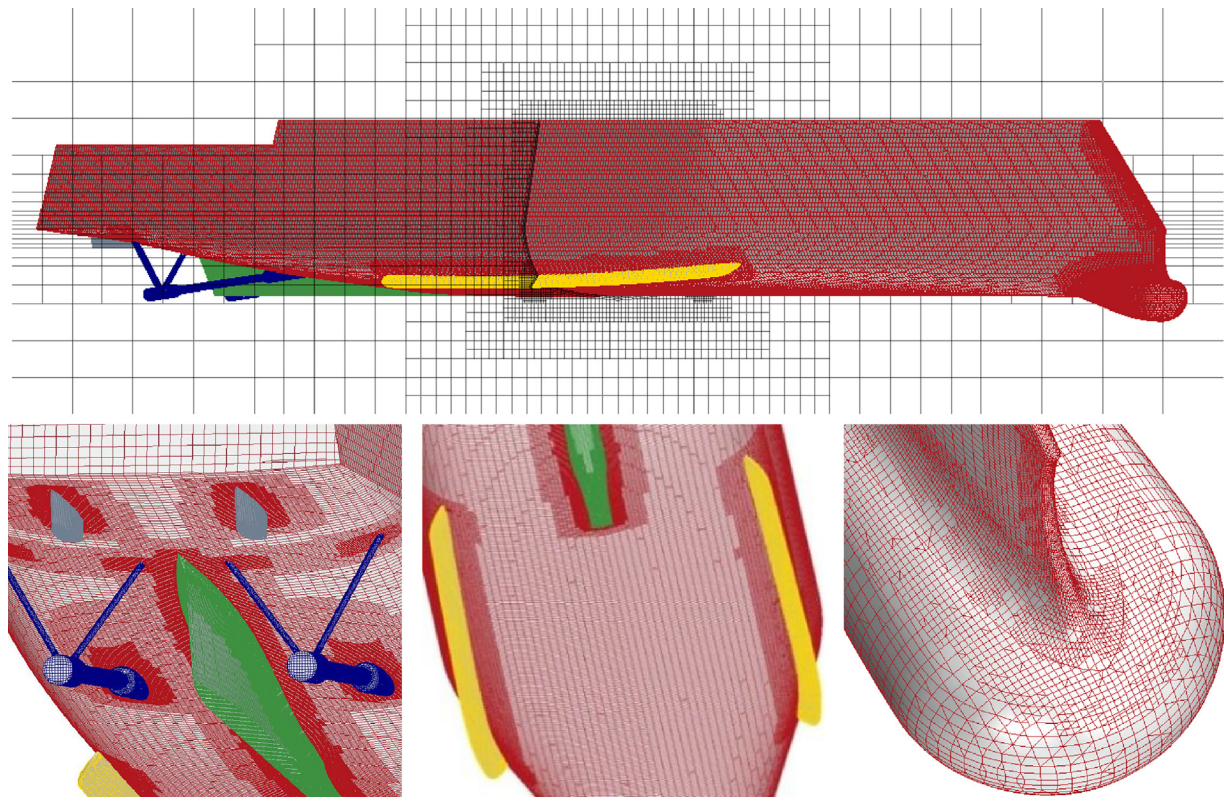


**Fig. 4.** CFD grids on the surface of hull and appendages.

**Table 2**

Grid convergence of static drift simulation with  $\beta = 10^\circ$ .

	X		Y		K		N	
	Pressure	Friction	Pressure	Friction	Pressure	Friction	Pressure	Friction
$S_1$	2.6398	4.1315	12.2676	0.1733	1.7681	0.0316	-13.9316	-0.0389
$S_2$	2.6858	4.1034	12.3425	0.1730	1.7599	0.0342	-13.8329	-0.0508
$S_3$	2.8237	4.0791	12.5685	0.1732	1.7664	0.0348	-13.8533	-0.0505
$\varepsilon_{21}\%S_1$	5.224	-0.588	1.842	0.102	0.368	1.951	0.146	-0.773
$\varepsilon_{32}\%S_1$	1.740	-0.680	0.611	-0.158	-0.463	8.042	-0.708	30.804
$R_G$	0.333	1.157	0.332	-1.554	-1.261	4.123	-4.841	-39.839
$Con.$	Mon.	Div.	Mon.	Osc.	Osc.	Div.	Osc.	Osc.
$P_G$	3.172	-	3.186	-	-	-	-	-
$C_G$	2.002	-	2.017	-	-	-	-	-
$U_G\%S_1$	2.611	-	0.918	0.079	0.232	-	0.354	15.402
$U_I\%S_1$	0.055	-	0.081	0.020	0.066	-	0.063	0.221

**Table 3**

Grid convergence of static heel simulation with  $\phi = 10^\circ$ .

	X		Y		K		N	
	Pressure	Friction	Pressure	Friction	Pressure	Friction	Pressure	Friction
$S_1$	1.8665	3.6492	0.1590	0.0085	-4.1559	0.0028	-0.3932	-0.0151
$S_2$	1.9198	3.6041	0.1761	0.0050	-4.1590	0.0022	-0.4030	-0.0174
$S_3$	2.0262	3.5606	0.1625	0.0014	-4.1548	0.0014	-0.4399	-0.0156
$\varepsilon_{21}\%S_1$	5.704	-1.194	-8.547	-41.433	-0.102	-28.188	9.370	-11.624
$\varepsilon_{32}\%S_1$	2.852	-1.235	10.713	-41.809	0.074	-20.115	2.509	15.249
$R_G$	0.500	1.034	-1.253	1.009	-0.730	0.714	0.268	-1.312
$Con.$	Mon.	Div.	Osc.	Div.	Osc.	Mon.	Mon.	Osc.
$P_G$	2.001	-	-	-	-	0.974	3.802	-
$C_G$	1.001	-	-	-	-	0.40	2.735	-
$U_G\%S_1$	3.135	-	5.356	-	0.051	110.407	4.100	7.625
$U_I\%S_1$	0.072	-	2.491	-	0.009	0.227	0.766	0.041

sets of grid referred to as coarse ( $S_3$ ), medium ( $S_2$ ), and fine ( $S_1$ ) are generated based on the refinement ratio of  $\sqrt{2}$ . Grid convergence study is performed for the static drift test with 1.37, 2.38

and  $4.40 \times 10^6$  grid points, and the static heel test with 1.37, 2.41 and  $4.43 \times 10^6$  grid points. Both forces and moments are divided into two components of pressure and friction. The results of gird

**Table 4**Time-step convergence of static drift simulation with  $\beta = 10^\circ$ .

	X		Y		K		N	
	Pressure	Friction	Pressure	Friction	Pressure	Friction	Pressure	Friction
$S_1$	2.6877	4.1081	12.4628	0.1814	1.7627	0.0370	-13.8420	-0.0554
$S_2$	2.6858	4.1034	12.3425	0.1730	1.7599	0.0342	-13.8329	-0.0508
$S_3$	2.7501	4.1074	12.4027	0.1504	1.7525	0.0254	-14.1993	-0.0314
$\varepsilon_{21}\%S_1$	2.393	0.097	0.483	-12.44	-0.420	-23.550	2.647	-35.093
$\varepsilon_{32}\%S_1$	-0.071	-0.115	-0.966	-4.67	-0.159	-7.691	-0.066	-8.248
$R_T$	-0.030	-1.195	-1.998	0.375	0.378	0.327	-0.025	0.235
$Con.$	Osc.	Osc.	Osc.	Mon.	Mon.	Mon.	Osc.	Mon.
$P_T$	-	-	-	1.414	1.404	1.614	-	2.089
$C_T$	-	-	-	1.664	1.647	2.063	-	3.255
$U_T\%S_1$	1.197	0.058	0.483	6.532	0.221	11.651	1.323	13.962
$U_f\%S_1$	0.179	0.007	0.201	0.032	0.071	0.059	0.148	0.157

**Table 5**Time-step convergence of static heel simulation with  $\phi = 10^\circ$ .

	X		Y		K		N	
	Pressure	Friction	Pressure	Friction	Pressure	Friction	Pressure	Friction
$S_1$	1.9239	3.5955	0.1809	0.0043	-4.1610	0.0019	-0.4120	-0.0153
$S_2$	1.9198	3.6041	0.1761	0.0050	-4.1590	0.0022	-0.4030	-0.0174
$S_3$	1.9317	3.6559	0.1640	0.0070	-4.1438	0.0022	-0.3479	-0.0171
$\varepsilon_{21}\%S_1$	0.619	1.440	-6.648	48.603	-0.364	-1.853	-13.376	-1.816
$\varepsilon_{32}\%S_1$	-0.216	0.239	-2.664	15.825	-0.048	14.890	-2.167	13.302
$R_T$	-0.349	0.166	0.401	0.326	0.132	-8.036	0.162	-7.326
$Con.$	Osc.	Mon.	Mon.	Mon.	Mon.	Osc.	Mon.	Osc.
$P_T$	-	2.588	1.319	1.619	2.924	-	2.626	-
$C_T$	-	5.014	1.495	2.071	6.588	-	5.172	-
$U_T\%S_1$	0.309	0.431	3.546	24.016	0.089	7.445	3.916	6.651
$U_f\%S_1$	1.047	0.001	9.910	0.931	0.030	0.582	4.889	0.260

convergence for the simulation of static drift and static heel tests are shown in [Tables 2 and 3](#), where 'Mon.', 'Osc.', and 'Div.' denote monotonic convergence, oscillatory convergence, and divergence, respectively. In the grid-spacing convergence study, the theoretical order of accuracy  $P_{Gest} = 2$  is adopted according to the spatial discretization scheme.

As shown in [Tables 2 and 3](#), the grid convergence can be achieved for all pressure components in the static drift and static heel simulations, while it shows divergence for some friction components in the both simulations. Concerning the grid uncertainty analysis for the simulation of static drift test, it can be observed that the friction components of surge force X and roll moment K fail to meet the convergence condition of  $R_G < 1$ . Hence, their uncertainty is unable to be estimated. Only the pressure components of surge force X and sway force Y show monotonic convergence with  $0 < R_G < 1$ , the others show oscillatory convergence with  $R_G < 0$ . For the pressure components of surge force X and sway force Y, the estimated order of accuracy  $P_G = 3.172$  and  $3.186$  are relatively larger than the theoretical order of accuracy  $P_{Gest}$ , suggesting that the solutions for them are far from the asymptotic range. For the simulation of static heel test, the friction components of surge force X and sway force Y do not meet the convergence condition. The pressure components of surge force X and yaw moment N and the friction component of roll moment K show monotonic convergence, while the rest show oscillatory convergence. The estimated order of accuracy  $P_G$  of the friction component of roll moment K and the pressure component of yaw moment N is 0.974 and 3.802 respectively, deviating from the theoretical order of accuracy  $P_{Gest}$  obviously. Only the solution of the pressure component of surge force X is close to the asymptotic range with  $P_G = 2.001$ . Overall, the pressure components show better grid convergence than the friction components, except for the sway force Y in static drift simulation. It indicates that the friction components are more affected by the grid uncertainty.

The iterative uncertainty  $U_f$  is also presented in [Tables 2 and 3](#), which is estimated on the basis of the convergence history of the

forces and moments in the solution with the fine grid. The iterative uncertainty  $U_f\%S_1$  is small for most variables, except for the pressure component of sway force Y in static heel simulation with  $U_f\%S_1 = 2.491$ .

### 3.3.2. Time step

In the time step convergence study, simulation is performed with the grid of medium density. Three sets of time step referred to as 0.04 s ( $S_3$ ), 0.02 s ( $S_2$ ), and 0.01 s ( $S_1$ ) are selected based on the refinement ratio 2. The time-step uncertainties for simulations of static drift and static heel tests are shown in [Tables 4 and 5](#). In the time-step convergence study, the theoretical order of accuracy  $P_{T_{test}} = 1$  is adopted according to the temporal discretization scheme.

As shown in [Tables 4 and 5](#), all the pressure components and friction components for both simulations achieve the time-step convergence, meeting the convergence condition of  $R_T < 1$ . Concerning the time-step convergence of static drift simulation, some force and moment components show oscillatory convergence, while others present monotonic convergence. For the pressure component of roll moment K and the friction components of sway force Y and roll moment K, the estimated order of accuracy  $P_T$  is close to the theoretical order of accuracy  $P_{T_{test}} = 1$ , suggesting that the solutions for them approach to the asymptotic range. However, the friction component of yaw moment N presents relatively larger  $P_T$ , indicating that the solution is far from the asymptotic range. For the static heel test simulation, the pressure component of surge force X and friction components of roll moment K and yaw moment N show oscillatory convergence, and the rest show monotonic convergence. In regard of the components with monotonic convergence, only the pressure component and friction component of sway force Y present reasonable  $P_T$ , approaching to the magnitude of  $P_{T_{test}}$ . The others show remarkable larger  $P_T$ , indicating that the solution for them is far from the asymptotic range. Overall, the pressure components of forces and moments present reasonable smaller time-step uncertainty  $U_T\%S_1$  than the friction

**Table 6**  
Matrix of EFD and CFD conditions.

Test	Approach	Yaw rate $r'$	Drift angle $\beta$ ( $^\circ$ )	Heel angle $\phi$ ( $^\circ$ )
Static drift	EFD [26] and CFD	0	0, 2, 5, 10, 15	0
CMT	EFD [26] and CFD	0.2, 0.4, 0.6	0, 2, 5, 10, 15	0
Static heel	EFD [27]	0	0	0, 10, 20
	CFD	0	0	0, 5, 10, 15, 20

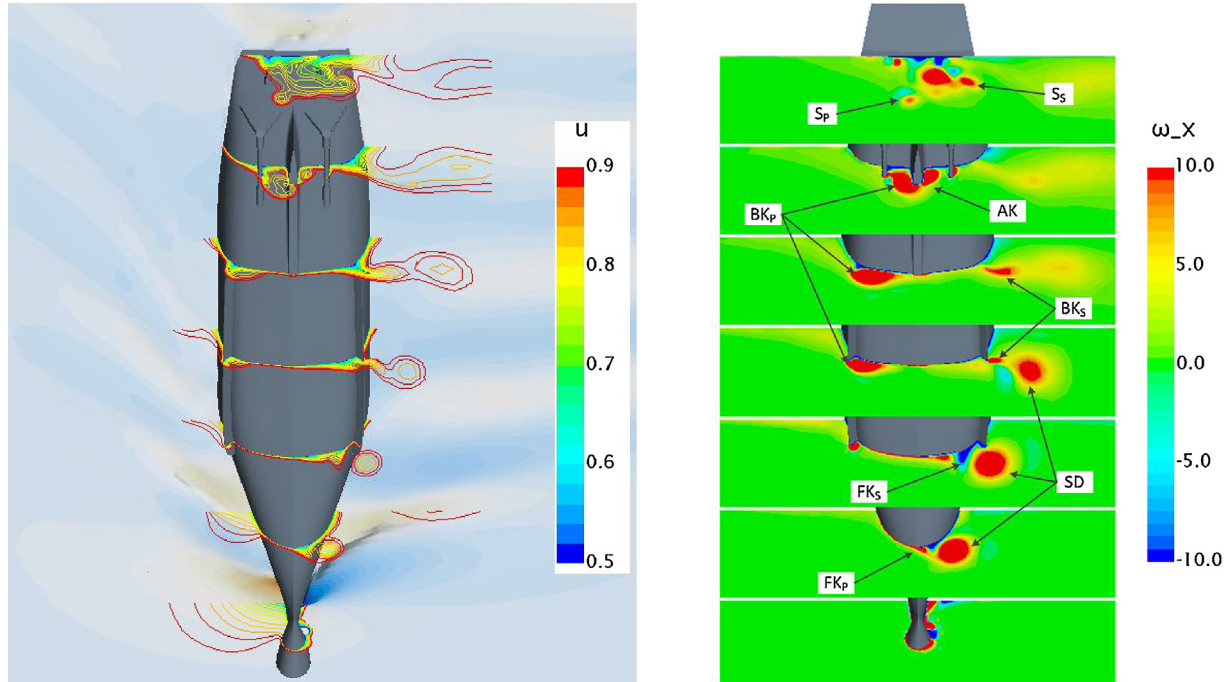


**Fig. 5.** Contours of axial velocity  $u$  (left) and axial vortex  $\omega_x$  (right): static drift with  $\beta = 15^\circ$ .

components for the static drift and static heel simulations, suggesting that the friction components are more affected also by the time-uncertainty.

The iterative uncertainty  $U_I$  is also presented in [Tables 4 and 5](#), which is estimated on the basis of the convergence history of the forces and moments in the solution with the fine time step. The iterative uncertainty  $U_I \times S_1$  is small for most components, except for the pressure component of sway force  $Y$  and yaw moment  $N$  in static heel simulation with  $U_I \times S_1 = 9.910$  and  $4.889$ , respectively.

Through the convergence study for the grid spacing and time step, it is found that the solution of hydrodynamic forces and moments is hard to reach the asymptotic range in maneuvers simulation overall. The components of pressure and friction in simulation show different sensitivity to the variation of grid spacing and time step. The friction component is more influenced by the uncertainty of grid and time step. Making tradeoff between the computation efficiency and accuracy, in the subsequent simulations of captive model tests the grid of medium density is used for spatial discretization, the total number of grid points is  $2.38 \times 10^6$  for the simulation of CMT and static drift test, and  $2.40\text{--}2.45 \times 10^6$  for the simulation of static heel test under different heel angles. Meanwhile, the time step of  $0.02$  s is used for temporal discretization.

#### 4. Numerical results

PMM test is widely used to determine the hydrodynamic derivatives for maneuverability estimation. However, it is well known that the hydrodynamic derivatives obtained from PMM test are remarkably dependent on the frequency and amplitude of motion

in the tests (Yasukawa and Yoshimura [\[32\]](#)), thus CMT and static drift test instead of PMM test are employed. In addition, it has been pointed out that the heel-induced hydrodynamic forces acting on ship are also important for motions of sway, yaw, and roll, especially for high speed vessels (Renilson and Manwarring [\[33\]](#)). The forces are caused by hydrodynamic force acting on the heeled asymmetric hull, and can be estimated by static heel simulation. In this study, simulations of the CMT, static drift and static heel tests are carried out for the ONRT model without propellers and rudders, and the hydrodynamic derivatives of hull are obtained. The configuration of the captive model tests is listed in [Table 6](#). All simulations are conducted under nominal speed  $Fr = 0.2$ . The heave and pitch motions in terms of dynamic sinkage and trim are free during simulation, which is in accordance with the physical model test condition.

##### 4.1. Local flow field

Since the experimental data of local flow field are not available in the literature, the qualitative analysis of the local flow field is presented here. The static drift of  $\beta = 15^\circ$ , steady turn of  $r' = 0.6$ , and static heel of  $\phi = 20^\circ$  are selected to clarify the effect of ship motion and attitude. Based on the ship-fixed coordinate system defined in section 3.2, the contours of axial velocity  $u$  and axial vortex  $\omega_x$  at 7 cross sections uniformly spaced extending from  $X_0 = -1.5$  m to 1.5 m are plotted in [Figs. 5–7](#). Only the flow under the waterline is demonstrated, and the variation of flow field along the longitudinal direction of the ship is visualized.

For the static drift case presented in [Fig. 5](#), it is shown that the flow field is highly disrupted by the interaction of cross flow and the existence of the ship model. There is a series of strong vortices,

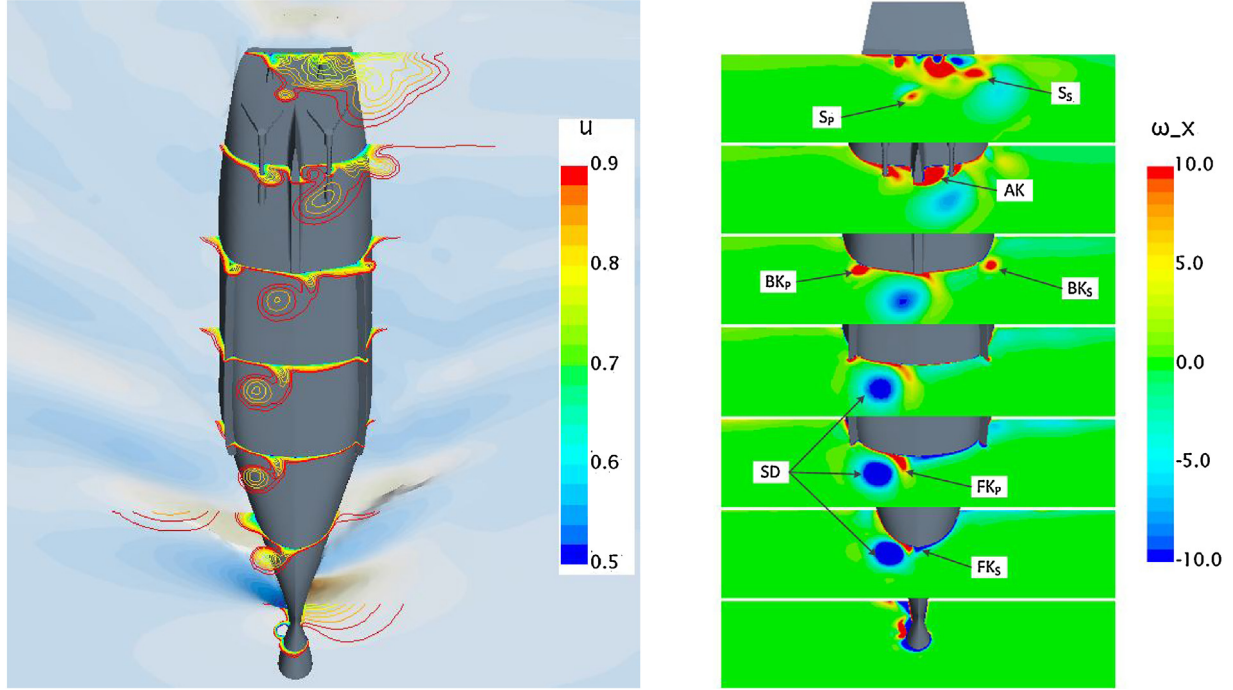


**Fig. 6.** Contours of axial velocity  $u$  (left) and axial vortex  $\omega_x$  (right): steady turn with  $r' = 0.6$ .

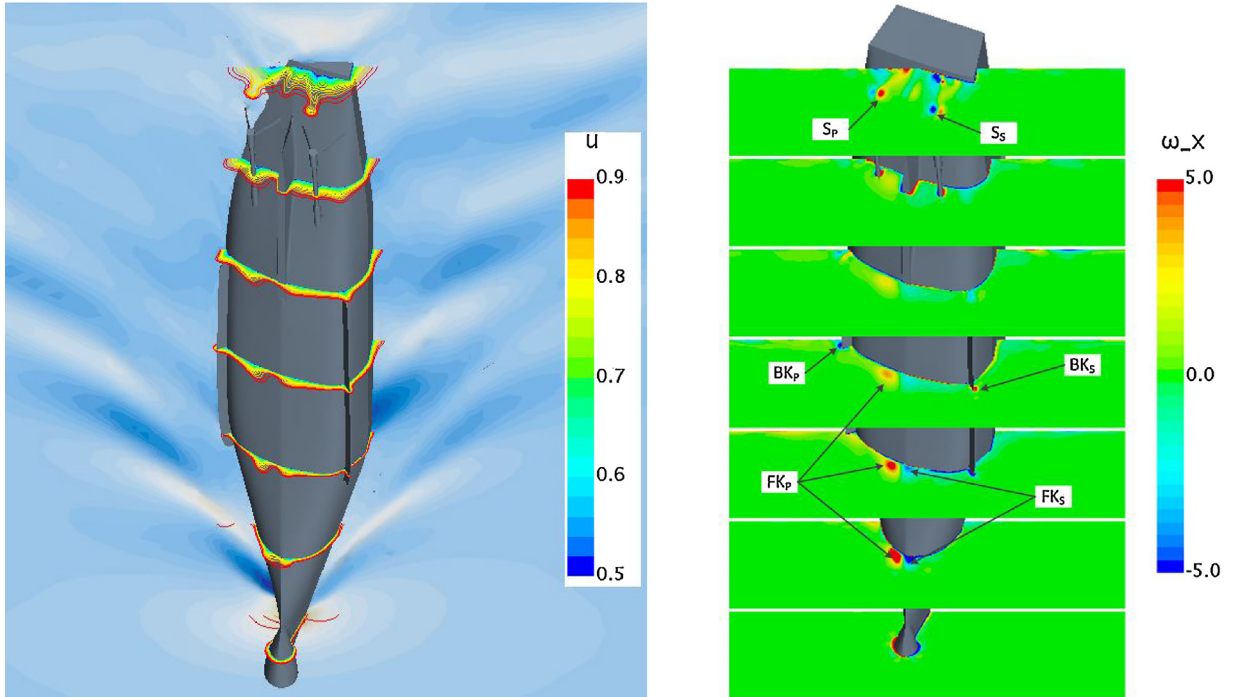


**Fig. 7.** Contours of axial velocity  $u$  (left) and axial vortex  $\omega_x$  (right): static heel with  $\phi = 20^\circ$ .

which is both visualized in the contours of  $u$  and  $\omega_x$ . Referring to the description of Sakamoto et al. [16], the major vortices are illustrated with sonar dome vortices (SD), fore-body keel vortices (FK), bilge keel vortices (BK), aft-body keel vortices (AK), and shaft vortices (S), where the subscripts of 'p', 's', represents portside, starboard, respectively. With the cross flow induced by drift angle, the major vortices of SD, BK, and FK are obviously deflected. However, it seems that the vortices of AK and S are with slighter deflection due to the flow-straightening effect. Observing from the stern, most vortices present counterclockwise rotation, while the vortex of  $FK_s$  shows

opposite rotation. The contours of  $u$  present a developing boundary layer around the hull, which is initially thin at the fore-body, and then grows thicker through the aft-body. Specially, the boundary layer presents asymmetry for the leeward and windward sides in the static drift case. For the leeward side, the boundary layer is rather thin on the fore-body and grows to be thicker with the interaction of  $BK_p$ . While, the boundary layer on the windward side of the whole body is thicker due to the interaction with SD,  $BK_s$ , and AK.

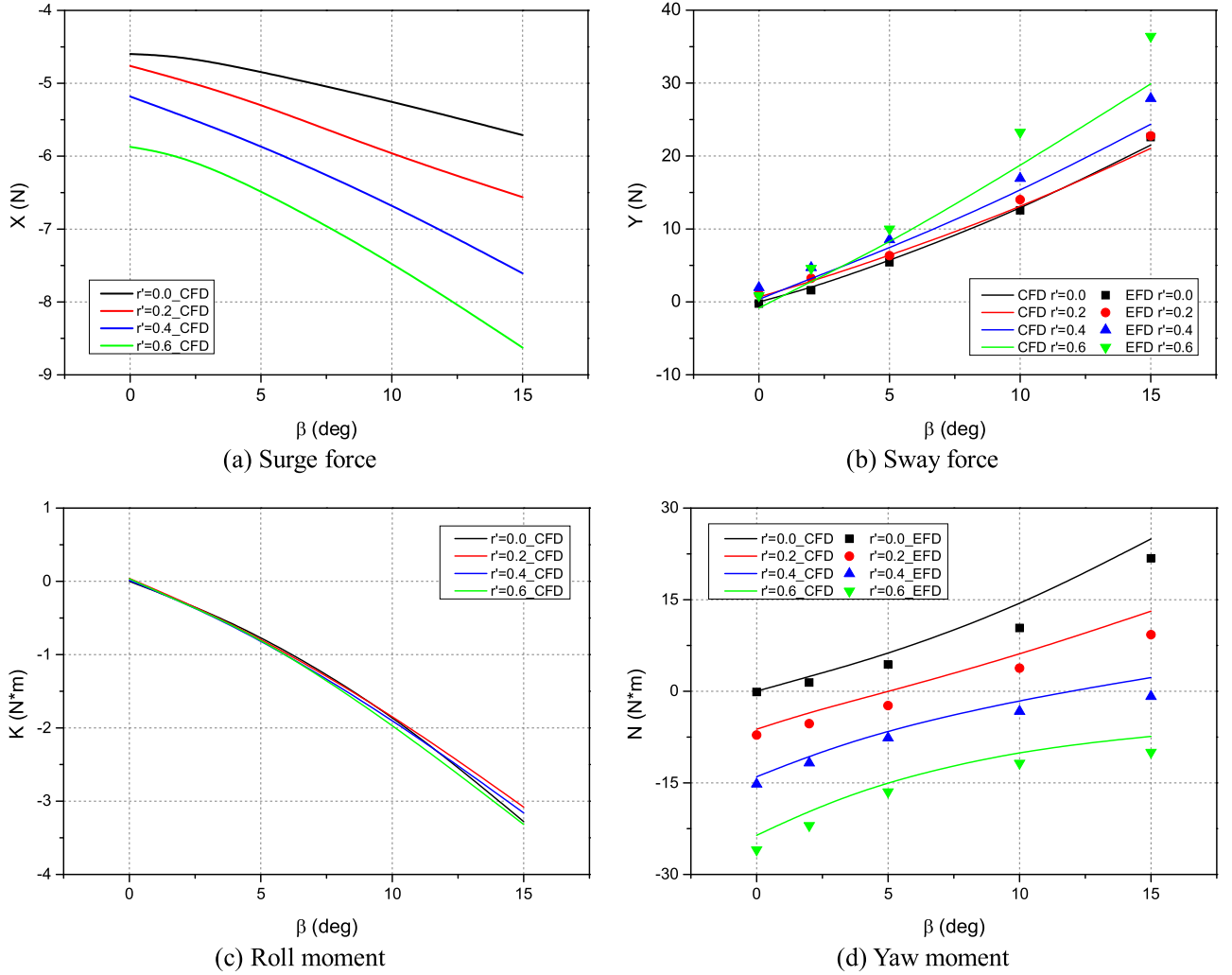


Fig. 8. Numerical results of CMT and static drift test simulations.

As shown in Fig. 6, the boundary layer and vortices distribution of steady turn case are different from those of the static drift case. For the direction of cross-flow in steady turn case, the leeward and windward sides are opposite for the fore-body and aft-body. The major vortices are distorted for the different local incident angles along the longitudinal axis of ship, and the vortices of SD and AK<sub>p</sub> present a clear curved path cross the ship hull. Particularly, the vortex of SD presents clockwise rotation, which is opposite to that of the static drift case. Correspondingly, the boundary layer is deformed with the effect of these distorted vortices, which is also thicker at the leeward side but thinner at the windward side. For the steady turn and static drift cases, the vortices distribution and the development of boundary layer show similar tend to that of Sakamoto et al. [16] with the similar ship type.

The boundary layer and vortices distribution of static heel case are presented in Fig. 7. It is shown that the strength of vortices is remarkably weaker than that of the static drift and steady turn. Only the vortex of AK<sub>p</sub> and AK<sub>s</sub> can be clearly observed, and the vortices show slight asymmetry due to the effect of heel angle. The boundary layer is thicker on the region near the vortices due to the effect of the vortices. Although there is no experiment validation for the flow field, the vortices distribution and development of boundary layer are predicted as expected. In addition, the shape of cross-section under the waterline is changed in static heel condition, which will influence the hydrodynamic and hydrostatic force acting on the ship model.

#### 4.2. Forces and moments

The computed hydrodynamic forces/moment from simulations of CMT and static drift test are shown in Fig. 8. Unfortunately, there is no sufficient experimental data for direct validation of the CFD results. Only the experimental data of sway force and yaw moment of CMT and static drift test for the ONRT model are available (Furukawa et al. [26]). For the sake of contrastive analysis, the orientation of forces and moments are transformed according to the coordinate system of horizontal body axes defined in Fig. 1. As shown in Fig. 8(b) and (d), the numerical results of sway force Y and yaw moment N are roughly consistent with the experimental data. The major deviation occurs at larger drift angle and yaw rate which may result in severe flow separation around ship hull. Moreover, it is shown that the surge force X and yaw moment N are highly affected by the sway velocity  $v$  and yaw rate  $r$ ; the sway force Y and roll moment K are sensitive to the sway velocity  $v$ , but seem to be irrelevant to the increase of yaw rate when  $r' \leq 0.2$ . To further investigate the relation between sway force Y and roll moment K, the relation under different yaw rate is plotted in Fig. 9; and the results of quantitative regression analysis for different polynomial order are listed in Table 7, where  $R$  is the Pearson correlation coefficient. It is shown that  $R^2$  improves only slightly with higher-order terms being considered for different value of  $r'$ , and the regression with first-order is quite precise with  $R^2 \approx 1.00$ . Therefore, the linear function of  $K = z_H Y$  is reasonable for this ship type.

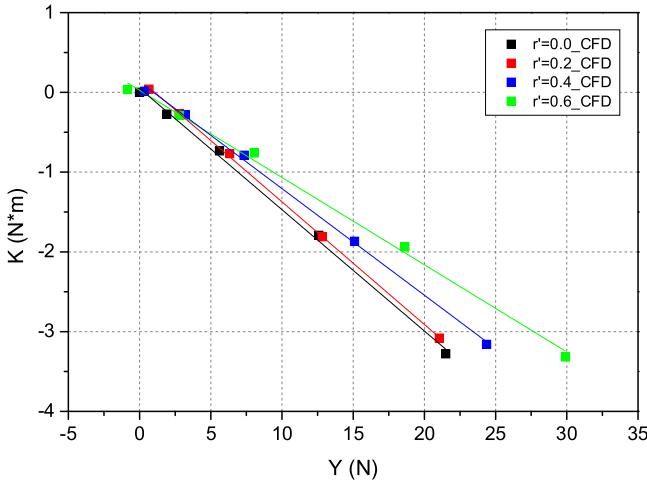


**Fig. 9.** Regression of roll moment and sway force in CMT and static drift test simulations.

The computed hydrodynamic forces and moments from simulation of static heel test are shown in Fig. 10. There is only experimental data of static heel test published by Sadat-Hosseini

**Table 7**  
Comparison of regressions under different polynomial order.

$r'$	$R^2$		
	First-order	Second-order	Third-order
0.0	0.99685	0.99975	0.99953
0.2	0.99954	0.99961	0.99984
0.4	0.99786	0.99918	0.99998
0.6	0.99523	0.99977	0.99979

et al. [27] for the ONRT model appended with skeg and bilge keels. It can be used for validation of the numerical results, since the effect of shafts and struts under straight ahead condition is negligibly small. As shown in Fig. 10(a) and (c), remarkable deviations are observed in the sway force  $Y$  and yaw moment  $N$ . The sway force  $Y$  is overestimated and the yaw moment  $N$  is underestimated in CFD simulation, while both show the consistent trend with EFD data. Actually, the deviations may have limited effect on the simulation of free maneuvers because of the rather small magnitude. In Fig. 10(b), the numerical results of roll moment  $K$  are in good agreement with the experimental data, showing promising prospect of the numerical method in prediction of roll motion. It is worth noting that the hydraulic moment  $mg\bar{GZ}(\phi)$  is also included in the computed roll moment.

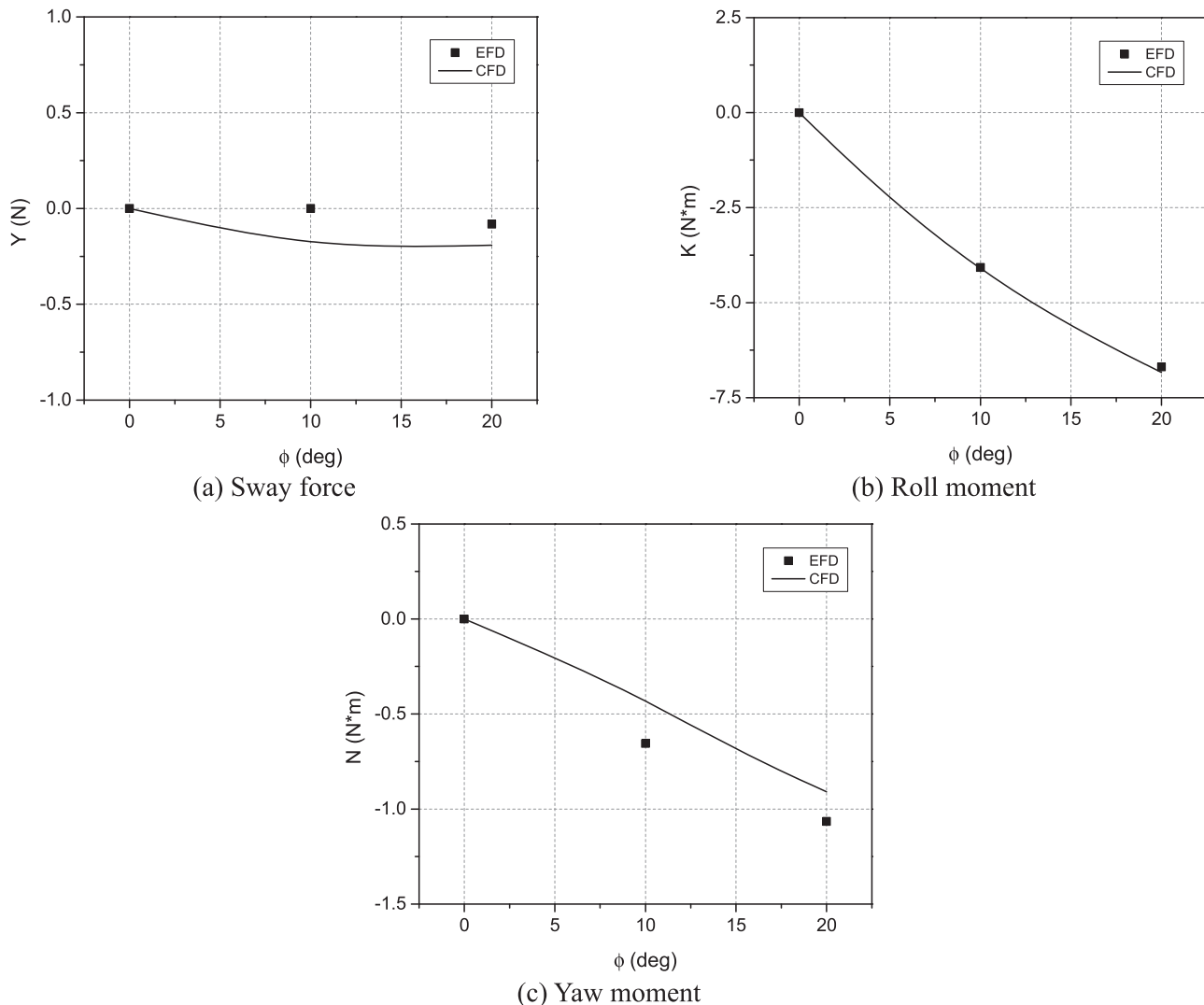


**Fig. 10.** Numerical results of static heel test simulation.

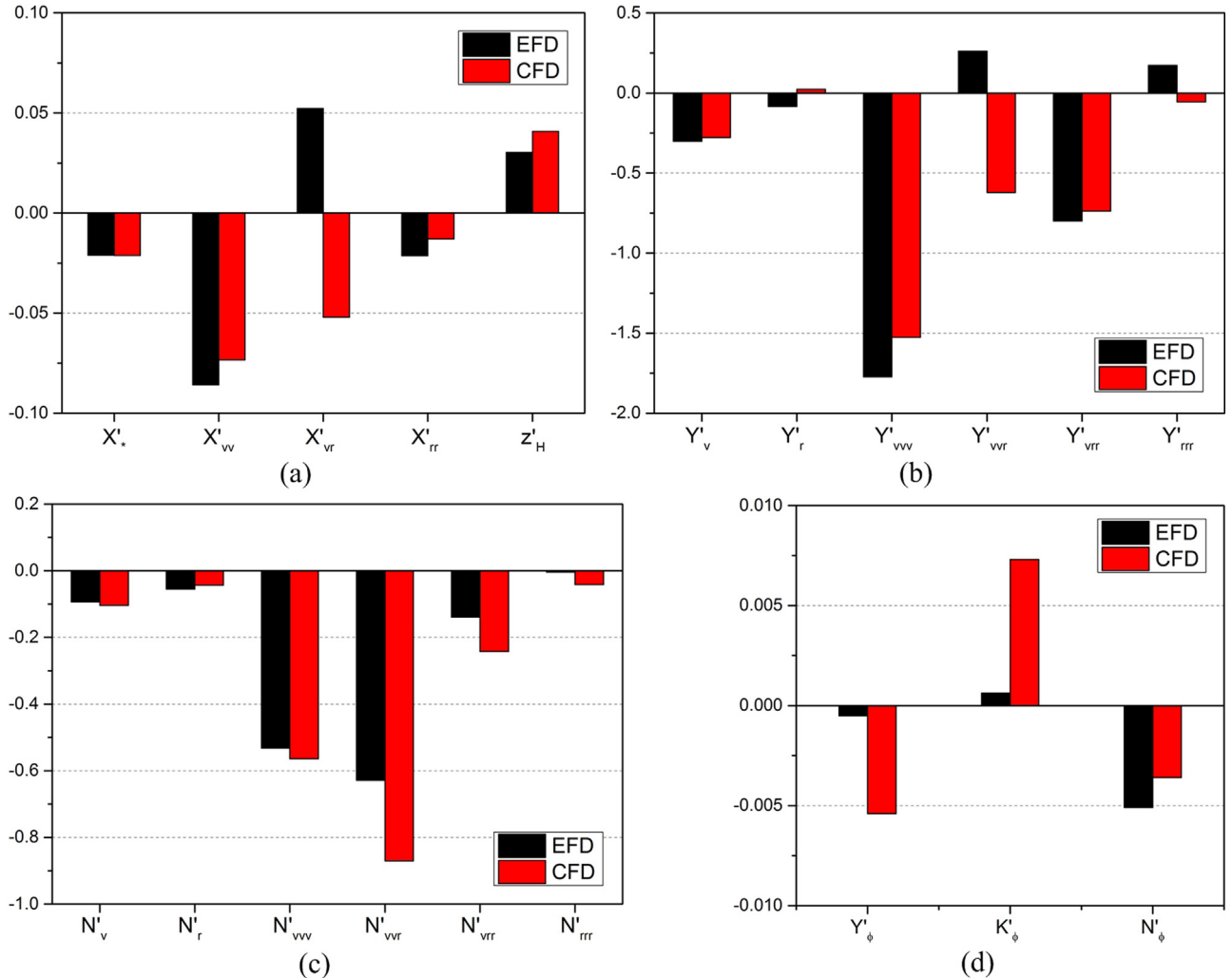


**Fig. 11.** Comparison of hydrodynamic derivatives obtained from EFD and CFD data.

**Table 8**  
Sub-models of hydrodynamic forces/moment for captive model tests

Test	Hydrodynamic force/moment	Sub-model
CMT and static drift	$X$	$a + bv^2 + cvr + dr^2$
	$Y, N$	$av + br + cv^3 + dv^2r + evr^2 + fr^3$
	$K$	$aY$
Static heel	$Y, K, N$	$a\phi$

#### 4.3. Hydrodynamic derivatives

For the captive model tests of CMT, static drift and static heel, the hydrodynamic forces/moment can be expressed by a series of polynomials. In order to improve the precision, the higher order terms are included in data fitting for forces/moment. The magnitude of heel angle  $\phi$  is relatively small during maneuvering in calm water, thus only the linear term is included in the mathematical model. The sub-models of the hydrodynamic forces/moment for the captive model tests are given in Table 8.

For the sake of contrastive analysis, the computed forces and moments are normalized with Eq. (20), and the dimensionless hydrodynamic derivatives are determined from the obtained data using least square method. As shown in Eqs. (2)–(4), the added mass terms are also included in the motion equations. They cannot be obtained from the static drift test and CMT simulations in

the present work. Here, the added mass  $m_x$  and  $m_y$  are taken from Araki et al. [29].

$$\left. \begin{aligned} X' &= \frac{X}{0.5\rho U^2 LT} \\ Y' &= \frac{Y}{0.5\rho U^2 LT} \\ K' &= \frac{K}{0.5\rho U^2 L^2 T} \\ N' &= \frac{N}{0.5\rho U^2 L^2 T} \end{aligned} \right\} \quad (20)$$

Comparisons of the hydrodynamic derivatives obtained from EFD data and CFD data are presented in Fig. 11, where the EFD results are also taken from Araki et al. [29]. In Fig. 11(a)–(c), the CFD results are obtained from the simulations of CMT and static drift test. The derivatives of  $X$  from CFD are of good agreement with that from EFD, except for  $X'_{vr}$ . The values of  $X'_{vr}$  from CFD and EFD data show opposite sign, indicating that the surge force  $X$  is underestimated in CFD computation. The derivatives of  $Y'_r$ ,  $Y'_{vvr}$ ,  $Y'_{vrr}$  show remarkable deviation, suggesting that there may be larger error for sway force  $Y$  prediction under turning condition. Fairly close agreement is obtained for the derivatives of yaw moment  $N$ , but error is obvious for non-linear terms, such as  $N'_{vvv}$ ,  $N'_{vvr}$ ,  $N'_{vrr}$ . The calculated  $z_H$ , the  $z$ -coordinate of the acting point of sway force, is close to that of EFD data.

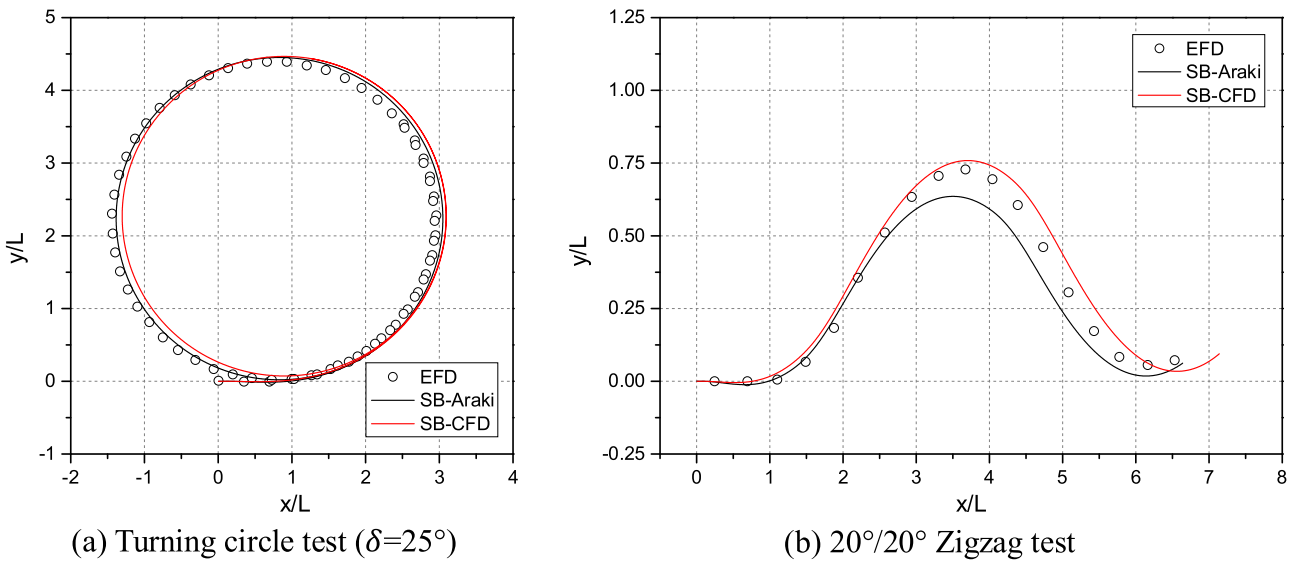


**Fig. 12.** Trajectories of free-running simulations ( $Fr=0.2$ ).

**Table 9**

Dimensionless inertia terms and linear damping coefficient (Araki et al. [29]).

Coefficient	Value	Source
$m'_x$	0.01307	Empirical formula
$m'_y$	0.10901	Strip theory
$J'_x$	0.000041	Free roll decay test
$J'_z$	0.00789	Strip theory
$K_p$	-0.2429	Free roll decay test

The derivatives derived from the data of static heel test simulation are presented in Fig. 11(d). The derivatives of  $Y'_\phi$ ,  $K'_\phi$  derived from CFD data show significant discrepancies from those of EFD data, while the error of  $N'_\phi$  is fairly small. In simulation of 4-DOF maneuvers, the trajectory is directly affected by sway force  $Y$  and yaw moment  $N$ . As shown in Fig. 11, the values of heel-related hydrodynamic derivatives are negligible compared with the hydrodynamic derivatives relating to sway velocity  $v$  and yaw rate  $r$ . Thus, the deviation in heel-related hydrodynamic derivatives may have negligible effect on the trajectory prediction of 4-DOF maneuvers. On the whole, the derivatives from CFD data show satisfactory agreement with those from EFD data, except for some high-order terms or those with small magnitude.

## 5. Free maneuvers simulation

Generally, the maneuvering performance of a ship can be evaluated by the turning circle and zigzag tests. Turning circle tests are performed to assess the vessel's turning ability, which is characterized by turning parameters such as advance, transfer and tactical diameter, etc. Zigzag tests are performed to assess the initial turning, yaw-checking and course-keeping abilities, the parameters obtained from these tests are the initial turning time, the overshoot angle, etc. In order to further verify the hydrodynamic derivatives from CFD data, turning circle test and zigzag test are simulated with system-based method. In the applied MMG model, the hydrodynamic derivatives obtained from CFD data in the last subsection are utilized. The adopted inertia terms and linear damping coefficient are listed in Table 9, which are taken from Araki et al. [29]. The relation between  $K_T$  and  $J$  is determined from the propeller open water characteristic data published at the Tokyo 2015 Workshop on CFD in Ship Hydrodynamics [34]. The remaining coefficients in the modules of propeller and rudder are given in Table 10. These parameters

**Table 10**

Parameters in the modules of propeller and rudder obtained from CFD.

Parameter	Value	Simulated test
$t_P$	0.090	Self-propulsion test
$W_P$	0.013	Self-propulsion test
$C_{YP}$	0.0319	Static drift test
$I'_P$	-0.4702	CMT
$t_R$	0.1563	Rudder force test
$a_H$	0.1957	Rudder force test
$z_{HR}/T$	0.8196	Rudder force test
$x_R/L$	-0.4459	Rudder force test
$x_H/L$	-0.3350	Rudder force test
$ v_{RP} /u_R$	0.0610	Rudder force test
$\varepsilon$	0.9050	Rudder force test
$\kappa$	0.6343	Rudder force test
$\eta$	0.6667	Rudder configuration
$\gamma_R^+$	0.7755	Static drift test
$\gamma_R^-$	0.3811	Static drift test
$I'_R^+$	-0.5137	CMT
$I'_R^-$	-0.9053	CMT

are obtained from CFD simulation of self-propulsion test, rudder force test, CMT, and static drift test with the full appended ship model. The detailed computation process is presented in Guo et al. [35].

To compare with the available EFD data, the turning circle test of  $\delta=25^\circ$  and  $20^\circ/20^\circ$  zigzag test under  $Fr=0.2$  are simulated by solving the 4-DOF MMG mathematical model with Runge-Kutta 4 (RK4) algorithm. The trajectories and kinematic parameters are compared with the free running data and simulation results published by Araki et al. [29], where the simulations are carried out with the hydrodynamic derivatives obtained from captive model tests and the empirical rudder force model.

The trajectory of turning circle test of  $\delta=25^\circ$  is presented in Fig. 12(a), and the comparison of related maneuverability parameters of advance, transfer, radius, and tactical diameter are given in Table 11. As shown in Fig. 12(a), both SB-Araki and SB-CFD show a lag in response to the steering on the initial stage of turning. It results in a slight overestimation of advance with 2.48%D for SB-Araki and 8.62%D for SB-CFD. The parameters of transfer, radius, and tactical diameter are underpredicted by SB-Araki with 4.97%D, 2.30%D, and 3.45%D, while overpredicted by SB-CFD with 4.59%D, 1.06%D, and 1.95%D, respectively. Overall, the trajectory of turning circle test is matched excellently by both simulations, and the SB-CFD presents a higher accuracy except for the prediction of advance.

**Table 11**

Maneuverability parameters of the free-running model tests.

Free maneuvers	Parameter	EFD	SB-Araki	E%D	SB-CFD	E%D
Turning circle test of $\delta = 25^\circ$	Advance ( $L$ )	2.82	2.89	-2.48	3.06	-8.62
	Transfer ( $L$ )	1.81	1.72	4.97	1.89	-4.59
	Radius ( $L$ )	2.17	2.12	2.30	2.19	-1.06
	Tactical diameter ( $L$ )	4.35	4.20	3.45	4.44	-1.95
20°/20° zigzag test	1st shoot angle ( $^\circ$ )	5.53	3.76	32.00	5.36	3.13
	2nd shoot angle ( $^\circ$ )	5.27	3.68	30.17	5.36	-1.63

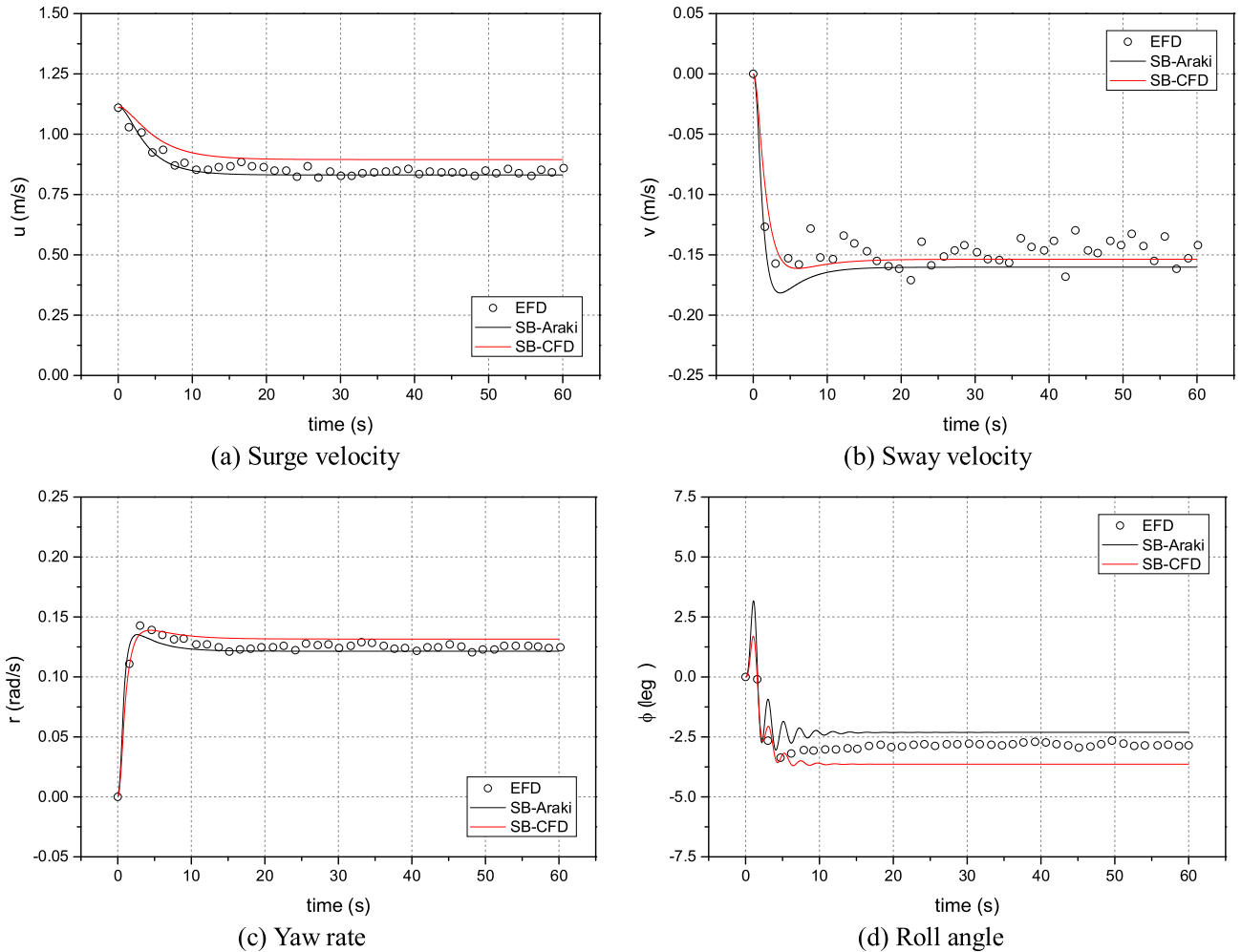
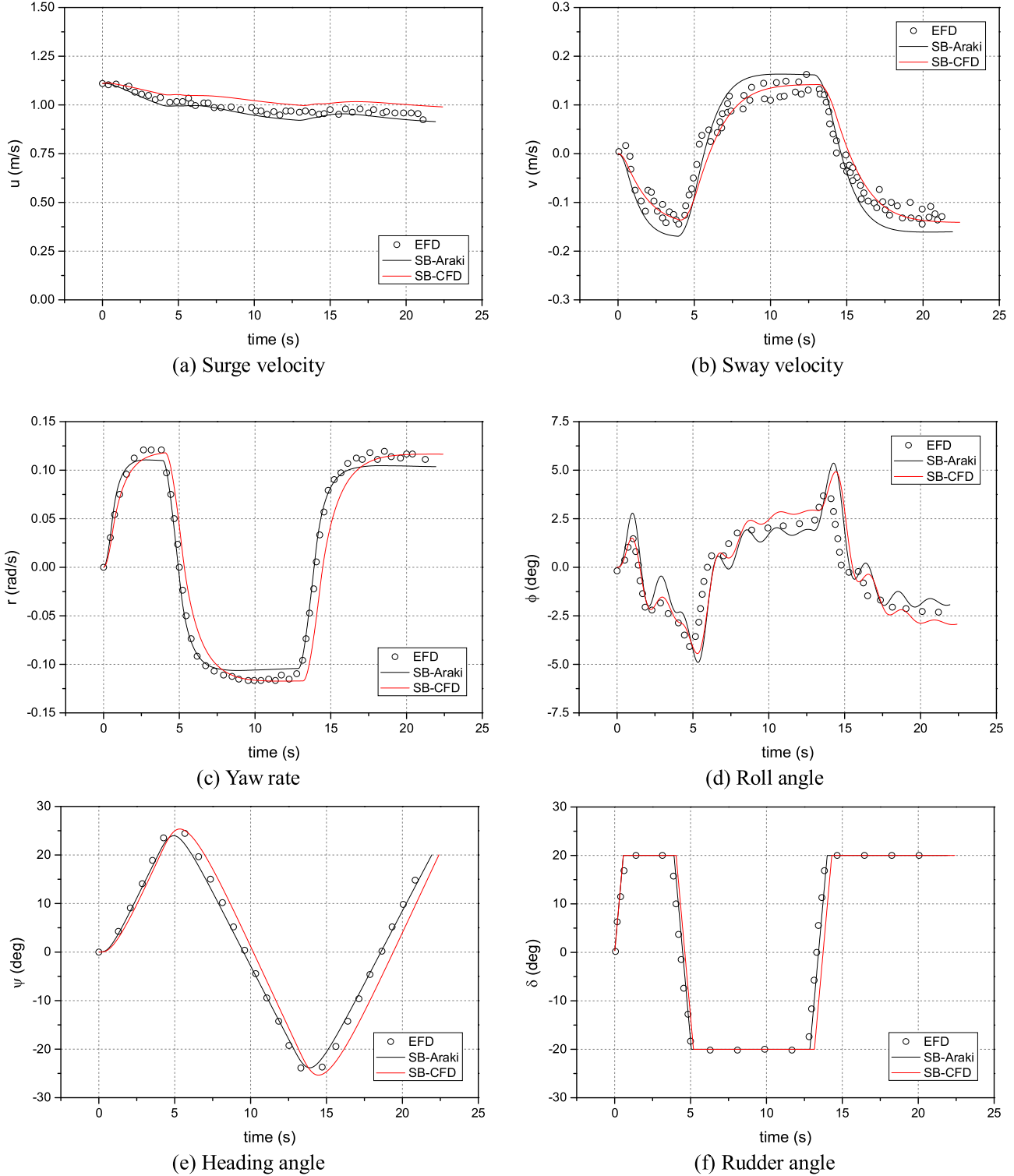


Fig. 13. Time histories of kinematic parameters during turning circle test ( $\delta = 25^\circ$ ,  $Fr = 0.2$ ).

The corresponding time histories of kinematic parameters during turning are presented in Fig. 13. As shown in Fig. 13(a)–(c), the overall trends of surge velocity, sway velocity, and yaw rate are reasonably matched by both simulations. At the initial stage of turning, SB-Araki presents similar change rate of velocities to the EFD data, while it is slightly underestimated by SB-CFD. When reaching the steady state of turning, the surge velocity and yaw rate are underestimated by SB-Araki, while overestimated by SB-CFD; the sway velocity is overestimated by both simulations. Fig. 13(d) depicts the time histories of roll angle during turning. Both simulations show similar trend with EFD data. There is remarkable oscillation in the simulations at the initial stage of turning, while the phenomenon is relative mild in the EFD data. The roll angle at the state of steady turning is underestimated by SB-Araki, but overestimated by SB-CFD. Although the errors are relative larger, the simulation results of roll motion are still acceptable because of the rather small magnitude of roll angle in steady turning condition (about 2.8°). It is

shown that both SB-Araki and SB-CFD present satisfactory accuracy in the prediction of kinematic parameters for the turning circle test of  $\delta = 25^\circ$ .

The trajectory of 20°/20° zigzag test is presented in Fig. 12(b). It is shown that there is some deviation between experimental data and simulation results. The trajectory of SB-CFD shows good agreement with EFD data, while there is a remarkable discrepancy between SB-Araki and EFD results. The corresponding time histories of kinematic parameters during zigzag maneuver are presented in Fig. 14. As shown in Fig. 14(a)–(c), the surge velocity, sway velocity, and yaw rate from both simulations present consistent trend with that of EFD. The surge velocity is dropping during the zigzag maneuver, which is slightly underestimated by SB-Araki but overestimated by SB-CFD. Differently, the sway velocity and yaw rate present periodical behavior approximately. SB-Araki overestimates the peak values of sway velocity but underestimates those of yaw rate; however, both of them are matched well by SB-CFD. The time



**Fig. 14.** Time histories of kinematic parameters during  $20^\circ/20^\circ$  zigzag test ( $Fr=0.2$ ).

histories of roll angle are presented in Fig. 14(d). It is shown that the changing trend of roll angle predicted by both simulations matches well with EFD data. On the other hand, both simulations present more dramatic fluctuation of roll angle than that of EFD data, especially just after the steering. The time histories of heading angle and rudder angle are plotted in Fig. 14(e) and (f), and the comparison of overshoot angles is given in Table 11. The changing trends of heading angle and rudder angle from both simulations appear

to be reasonably close to that of EFD. The peak values of heading angle are remarkably underestimated by SB-Araki while matched excellently by SB-CFD. As shown in Table 11, 1st and 2nd overshoot angles are underestimated by SB-Araki with 32.00%D and 30.17%D, respectively. In contrast, SB-CFD presents much higher accuracy in the prediction of overshoots, with error of 3.13%D for the 1st overshoot angle and  $-1.63\%$ D for the 2nd overshoot angle. Overall, SB-CFD presents satisfactory accuracy in the prediction of trajec-

tory and kinematic variables for the simulated free maneuvers, indicating the validity of the hydrodynamic derivatives and hull-propeller-rudder interaction coefficients obtained by CFD method.

## 6. Conclusions

In the present study, a system-based prediction of 4-DOF ship maneuvering is implemented for the unconventional ship type ONR tumblehome, where the hydrodynamic derivatives of hull in the 4-DOF MMG model are determined by simulation of CMT, static drift and heel tests using the RANS solver in STAR-CCM+. The convergence study is carried out for the simulation of selected static drift and static heel test, and the influence of grid spacing and time step on the numerical results is clarified. A series of simulations of CMT, static drift and static heel tests are carried out. The vortices distribution and development of boundary layer are demonstrated for the selected cases to visualize the effect of ship motion and attitude on the flow. Parts of computed force and moment are compared with available experimental data, showing satisfactory agreement. Further, the hydrodynamic derivatives derived from the computed forces and moments are compared with those from experimental data published in literature, exhibiting fairly close agreement, except for some high-order terms or those with small magnitude.

The turning circle test of  $\delta=25^\circ$  and  $20^\circ/20^\circ$  zigzag test are simulated by solving the 4-DOF MMG model with the computed hydrodynamic derivatives and hull-propeller-rudder interaction coefficients. For the turning circle test and zigzag test, it is shown that the trajectories and time histories of kinematic variables from the simulations are in good agreement with the experimental data. Remarkable deviation occurs in the prediction of roll angle, which may be caused by simplification of the mathematical model and/or inaccurate estimation of the inertial terms. However, the deviation of simulation is acceptable because of the small roll angle in free maneuvers. The comparison of typical maneuverability parameters demonstrates the promising applicability of the present system-based method coupled with CFD simulation of captive model tests in prediction of 4-DOF maneuvering for the unconventional ship type ONRT.

## Acknowledgments

This work is financially supported by the National Natural Science Foundation of China [Grant number 51309152] and the Fund of the State Key Laboratory of Ocean Engineering of Shanghai Jiao Tong University for Independent Researches [Grant number GKZD010068].

## References

- [1] IMO Res MSC.137 (76), Standards for ship manoeuvrability, 2002.
- [2] IMO MSC/Circ.1053, Explanatory notes to the standards for ship manoeuvrability, 2002.
- [3] H. Yasukawa, Y. Yoshimura, Roll-coupling effect on ship maneuverability, *Ship Technol. Res.* 61 (1) (2014) 16–32.
- [4] O. el Moctar, U. Lantermann, P. Mucha, et al., RANS-based simulated ship maneuvering accounting for hull-propulsor-engine interaction, *Ship Technol. Res.* 61 (3) (2014) 142–161.
- [5] R. Broglia, G. Dubbioso, D. Durante, et al., Simulation of turning circle by CFD: Analysis of different propeller models and their effect on maneuvering prediction, *Appl. Ocean Res.* 39 (2013) 1–10.
- [6] R. Broglia, G. Dubbioso, D. Durante, et al., Turning ability analysis of a fully appended twin screw vessel by CFD. Part I: Single rudder configuration, *Ocean Eng.* 105 (2015) 275–286.
- [7] G. Dubbioso, D. Durante, R. Broglia, Zig-zag maneuver simulation by CFD for a tanker like vessel, in: 5th International Conference on Computational Methods in Marine Engineering, Hamburg, Germany, 2013.
- [8] P.M. Carrica, F. Ismail, M. Hyman, et al., Turn and zigzag maneuvers of a surface combatant using a URANS approach with dynamic overset grids, *J. Mar. Sci. Technol.* 18 (2) (2013) 166–181.
- [9] M.A. Abkowitz, Lectures on ship hydrodynamics – steering and manoeuvrability, in: Hydro-og Aerodynamisk Laboratorium, Report No. Hy-5, Lyngby, Copenhagen, Denmark, 1964.
- [10] M. Hirano, J. Takashina, A calculation of ship turning motion taking coupling effect due to heel into consideration, *J. West-Japan Soc. Naval Archit.* 59 (1980) 71–81.
- [11] K.H. Son, K. Nomoto, On the coupled motion of steering and rolling of a high-speed container ship, *Naval Archit. Ocean Eng.* 20 (1982) 73–83.
- [12] N. Umeda, H. Hashimoto, Qualitative aspects of nonlinear ship motions in following and quartering seas with high forward velocity, *J. Mar. Sci. Technol.* 6 (3) (2002) 111–121.
- [13] P. Atsavapranee, R. Miller, C. Dai, et al., Steady-turning experiments and RANS simulations on a surface combatant hull form (Model#5617), in: 28th Symposium on Naval Hydrodynamics, Pasadena, USA, 2010.
- [14] C. Dai, R. Miller, URANS simulation of an appended hull during steady turn with propeller represented by an actuator disk model, in: 30th International Conference on Ocean, Offshore and Arctic Engineering, Rotterdam, Netherlands, 2011.
- [15] N. Sakamoto, P.M. Carrica, F. Stern, URANS simulations of static and dynamic maneuvering for surface combatant: part 1. Verification and validation for forces, moment, and hydrodynamic derivatives, *J. Mar. Sci. Technol.* 17 (4) (2012) 422–445.
- [16] N. Sakamoto, P.M. Carrica, F. Stern, URANS simulations of static and dynamic maneuvering for surface combatant: part 2: Analysis and validation for local flow characteristics, *J. Mar. Sci. Technol.* 17 (4) (2012) 446–468.
- [17] R.R. Shenoi, P. Krishnankutty, R.P. Selvam, et al., Prediction of maneuvering coefficients of a container ship by numerically simulating HPMM using RANSE based solver, in: 3rd International Conference on Ship Manoeuvring in Shallow and Confined Water, Ghent, Belgium, 2013.
- [18] R.R. Shenoi, P. Krishnankutty, Study of manoeuvrability of container ship by static and dynamic simulations using a RANSE-based solver, *Ships Offshore Struct.* (2014) 1–19.
- [19] P. Mucha, O. el Moctar, Maneuvering prediction for a large tanker through virtual captive model tests, in: SIMMAN 2014, Workshop on Verification and Validation of Ship Maneuvering Simulation Methods, Copenhagen, Denmark, 2014.
- [20] S.M. Mousaviraad, S.S. Cook, P.M. Carrica, et al., Complimentary EFD and CFD on effects of headwinds on towing tank resistance and PMM tests for ONR tumblehome, in: 29th Symposium on Naval Hydrodynamics, Gothenburg, Sweden, 2012.
- [21] H. Miyazaki, M. Ueno, Y. Tsukada, Numerical study about effects of stern skeg on course stability, in: 21st International Offshore and Polar Engineering Conference, Hawaii, USA, 2011.
- [22] Y.J. Sung, S.H. Park, K.S. Ahn, et al., Evaluation on deep water manoeuvring performances of KVLCC2 based on PMM test and RANS simulation, in: SIMMAN 2014, Workshop on Verification and Validation of Ship Maneuvering Simulation Methods, Copenhagen, Denmark, 2014.
- [23] A. Cura-Hochbaum, S. Uharek, Prediction of the manoeuvring behaviour of the KCS based on virtual captive tests, in: SIMMAN 2014, Workshop on Verification and Validation of Ship Maneuvering Simulation Methods, Copenhagen, Denmark, 2014.
- [24] N. Sakamoto, K. Kume, Zig-zag simulations of KVLCC2 by CFD-systems based maneuvering prediction method, *Lectures of the Japan Society of Naval Architects and Ocean Engineers* 19 (2014) 227–230.
- [25] S.K. Lee, M. Fujino, T. Fukasawa, A study on the manoeuvring mathematical model for a twin-propeller twin-rudder ship, *J. Soc. Naval Archit. Jpn.* 163 (6) (1988) 109–118.
- [26] T. Furukawa, N. Umeda, A. Matsuda, et al., Effect of hull form above calm water plane on extreme ship motions in stern quartering waves, in: 29th Symposium on Naval Hydrodynamics, Gothenburg, Sweden, 2012.
- [27] H. Sadat-Hosseini, P. Carrica, F. Stern, et al., CFD, system-based and EFD study of ship dynamic instability events: surf-riding, periodic motion, and broaching, *Ocean Eng.* 38 (1) (2011) 88–110.
- [28] Y. Sanada, K. Tanimoto, K. Takagi, et al., Trajectories for ONR Tumblehome maneuvering in calm water and waves, *Ocean Eng.* 72 (2013) 45–65.
- [29] M. Araki, H. Sadat-Hosseini, Y. Sanada, et al., Estimating maneuvering coefficients using system identification methods with experimental, system-based, and CFD free-running trial data, *Ocean Eng.* 51 (2012) 63–84.
- [30] F. Stern, R.V. Wilson, H. Coleman, et al., Verification and validation of CFD simulations, in: IIHR Report No. 407, Iowa Institute of Hydraulic Research, The University of Iowa, 1999.
- [31] T. Xing, F. Stern, Factors of safety for Richardson extrapolation, *J. Fluids Eng.* 132 (6) (2010), 061403.
- [32] H. Yasukawa, Y. Yoshimura, Introduction of MMG standard method for ship maneuvering predictions, *J. Mar. Sci. Technol.* 20 (1) (2015) 37–52.
- [33] M.R. Renilson, T. Manwarring, An investigation into roll/yaw coupling and its effect on vessel motions in following and quartering seas, in: 7th International Conference on Stability and Ocean Vehicles, Launceston, Australia, 2000.
- [34] Tokyo 2015, A Workshop on CFD in Ship Hydrodynamics, 2015, <http://www.t2015.nmri.go.jp/>.
- [35] H.P. Guo, Z.J. Zou, Y. Liu, et al. Investigation on hull-propeller-rudder interaction by RANS simulation of captive model tests for a twin-screw ship. To be submitted.